JOURNAL OF GEOPHYSICAL RESEARCH, VOL. 98, NO. C6, PAGES 10,171–10,184, JUNE 15, 1993

Characteristics of the Summer 1987 Flow Field in the Ionian Sea

KOSTAS NITTIS

Laboratory of Meteorology and Oceanography, Department of Applied Physics, University of Athens, Athens, Greece

NADIA PINARDI

Istituto per lo Studio dello Metodologie Geofisiche Ambientali, Consiglio Nazionale delle Ricerche, Modena, Italy

ALEX LASCARATOS

Laboratory of Meteorology and Oceanography, Department of Applied Physics, University of Athens, Athens, Greece

We present an extensive analysis of the first complete data set in the northern Ionian Sea collected during the Physical Oceanography of the Eastern Mediterranean (POEM) general circulation survey of September 1987. A four water mass structure of the basin is found to be represented by a first internal baroclinic Rossby radius of deformation of 11.8 km. The horizontal correlation scales decrease with depth, and the subsurface flow is dominated by anticyclonic gyres. Large-scale circulation trends of the temperature and salinity covariance matrices are compensated below 200 m, and only the gyre scales (~100 km) persist at intermediate and deep levels. The empirical orthogonal functions of the data set show that an horizontal scale separation exists between the first and higher vertical modes of the dynamic height field.

1. INTRODUCTION

The Ionian Sea is the largest in volume (~10^6 km^3) basin of the eastern Mediterranean, with depths that exceed 4000 m (maximum 5100 m in the Hellenic Trench). It is surrounded by the coasts of southern Italy, western Greece, and north Africa (Figure 1*a*). To the west it communicates with the western Mediterranean Sea through the Strait of Sicily (135 km wide with sill depth of 330 m), to the east with the Levantine basin through the Cretan passage (300 km wide with an average depth of 2000 m), and to the north with the Adriatic Sea through the Strait of Otranto (75 km wide with average depth of 300 m). Finally, it communicates with the Aegean Sea through the Kithira Strait (70 km wide with a maximum depth of 700 m).

The Mediterranean is a concentration basin, i.e., evaporation exceeds precipitation and runoff, and thus the conservation of mass and salinity is controlled by the inflow of fresh (36.2 psu and 15°C) Atlantic water and the outflow of saltier Mediterranean water through the straits of Gibraltar. The Strait of Sicily plays for the eastern Mediterranean the same controlling role as does Gibraltar for the whole Mediterranean. The Atlantic water that reaches the Strait of Sicily is modified (it is then more salty), but it conserves its characteristics and is observed as a subsurface salinity minimum even in the western Levantine basin [*Ozsoy et al.*, 1989]. In the Ionian Sea the signal of Atlantic water is expected to be especially strong during summer, when the evaporation is intense and the mixing is low.

Another characteristic water mass of the eastern Mediterranean is the so called Levantine Intermediate Water (LIW) that is usually traced as a salinity maximum (around 39 psu in the Levantine) at intermediate depths (100–400 m). It is formed in the Levantine basin (mainly in the Rhodes cyclonic gyre area) during winter by convective mixing caused by strong and dry continental winds [*Ovchinnikov and Plakhin*, 1984]. Recent measurements have shown that LIW is abundant also in the southern Levantine basin [*Robinson et al.*, 1991; *Ozsoy et al.*, 1989]. This water mass sinks down to a depth of 300–400 m and then spreads throughout the Mediterranean Sea. In the Ionian Sea it is traced in the same depths but with modified characteristics (less saline and cooler).

Finally, the third characteristic water mass in the area is the eastern Mediterranean deep waters that lie below the LIW. They are characterized by salinity of 38.7 psu and temperature of 13.6°C. The origin of these waters is believed to be the north and south Adriatic Sea [*Ovchinnikov*, 1984; *Schlitzer et al.*, 1991], where the conditions during winter are appropriate for their formation. According to *Miller* [1963], the Aegean Sea could also contribute to the Eastern Mediterranean Deep Water but this contribution should, according to *Schlitzer et al.* [1991], be very small.

Our knowledge of the general circulation characteristics of the Ionian Sea is limited to the circulation maps provided by *Ovchinnikov and Fedoseyev* [1965] for the whole Mediterranean. The upper layers winter circulation in this area is characterized by a large cyclonic gyre formed by the Atlantic water that enters from the Strait of Sicily. An eastward circulation in the southern Ionian sea seems to carry this water towards the Levantine basin. The summer circulation pattern is completely different because a large anticyclonic gyre is now present in this area. The eastward flow of Atlantic water seems to be limited at the northern part of the Cretan passage, while in the south Ionian the flow is westward.

During the past few years, a number of coordinated cruises in the framework of the Physical Oceanography of the Eastern Mediterranean (POEM) surveys [*UNESCO*,

Paper number 93JC00451.
0148-0227/93/93JC-00451$05.00

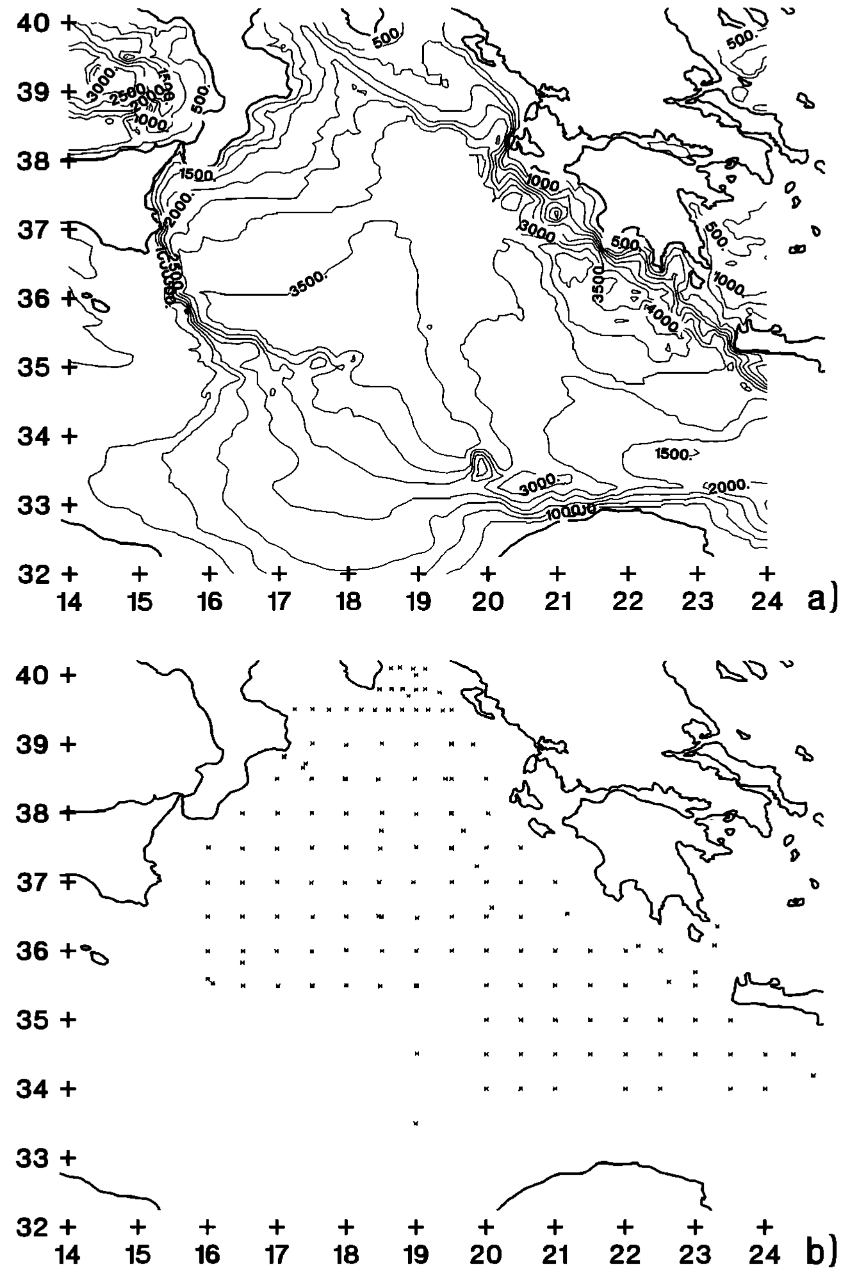

Fig. 1. Northern Ionian Sea (*a*) bathymetry (the contour interval is 500 m) and (*b*) station distribution.

1984] made available a basin wide high-resolution (for general circulation studies), reliable data set of oceanographic parameters in the eastern Mediterranean. A recent analysis of these data [*Robinson et al.*, 1991; *Ozsoy et al.*, 1989] has revealed the presence of circulation patterns far more complicated than the one presented in previous works.

Our work concentrates upon the most complete of the POEM surveys done in the northern Ionian basin (POEM V, September 1987). This data set has been intercalibrated and analyzed previously [*Pinardi*, 1988; *Robinson et al.*, 1991], but only horizontal mapping was considered. In our work we analyze for the first time the water mass structure of the flow, together with its correlation scales both horizontal and vertical. A brief description on the data used is given in section 2, while in section 3 a water mass analysis is presented. In the same section the first three baroclinic modes are computed, and the levels capable of reproducing the structure of these modes are chosen. In section 4 the estimation of the correlation matrices of the various parameters is presented together with the calculation of the correlation function that was used for the objective analysis of the data. The mapping of dynamic height, temperature, and salinity fields at different levels is given in section 5, and the resulting features are discussed. In section 6 we give an empirical orthogonal function (EOF) representation of the data, studying the vertical structure of the dynamic height, temperature and salinity fields. Finally, in section 7 we summarize the main conclusions of this work.

2. THE DATA SET

The present study is based upon the analysis of hydrological (conductivity-temperature-depth, CTD) data collected

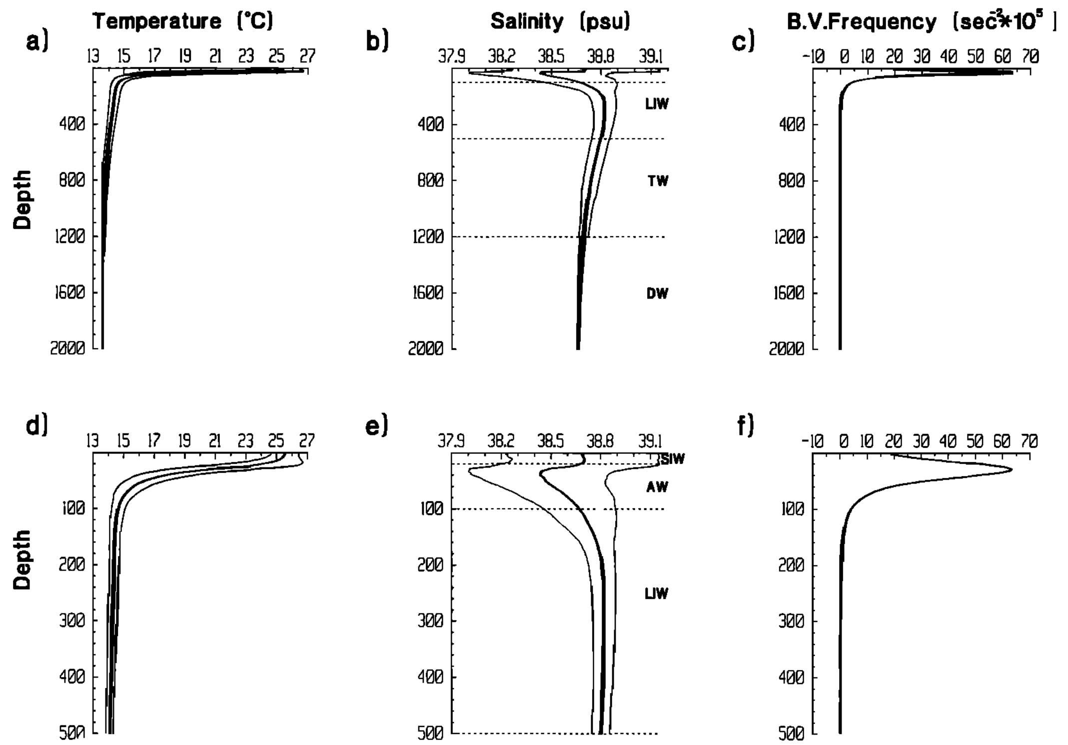

Fig. 2. Station averages of (*a*) temperature, (*b*) salinity, and (*c*) Brunt-Väisälä frequency for 0- to 2000-m depth, and (*d*) temperature, (*e*) salinity, and (*f*) Brunt-Väisälä frequency from 0- to 500-m depth. Thin lines represent average plus and minus the standard deviation.

during late summer (September) 1987 in the Ionian Sea, within the framework of POEM V general circulation survey [*Malanotte-Rizzoli and Robinson*, 1988]. The data were sampled on an almost regular 0.5° grid (Figure 1*b*), while a denser grid was used in the north Ionian Sea near the Strait of Otranto. Three research institutes participated in the data acquisition in this area: (1) the Greek National Center of Marine Research with R/V *Aegaio* covered the area east of 19°E (64 stations, September 7–30, 1987) using a SBE-9 Sea Bird CTD profiler, (2) the Istituto di Ricerche sulla Pesca Marittima (IRPEM, Ancona, Italy) and the Instituto Sperimentale Talassografico (IST, Trieste, Italy) of the Consiglio Nazionale delle Ricerche (CNR) covered the area west of 19°E and the Strait of Otranto (81 stations, September 1–18, 1987) with R/V *Bannock* using a Neil Brown CTD, and (3) the Osservatorio Geofisico Sperimentale (OGS, Trieste, Italy) sampled 22 stations on a nonregular grid (September 2–11, 1987) inside the area using a Neil Brown profiler. Each institute performed quality controls (sensors calibrations, comparison with salinometer measurements of water samples, etc.) of the measurements, and corrections were made when necessary.

The common stations between pairs of the three data sets were used for intercalibration tests during the POEM Mapping Group meeting that took place at Modena, Italy [*Pinardi*, 1988]. Since measurements at common stations were not simultaneous, intercomparisons were carried out on averages of data deeper than 1000 m where the water properties are expected to be time-invariant (at least on time scales of a few days). This procedure showed that there is no need for correction to any of the three data sets (for both salinity and temperature measurements).

3. Water Mass Analysis

We present here a classical water mass analysis by looking at the station-averaged vertical profiles of temperature, salinity and Brunt-Väisälä frequency. In Figure 2 the temperature average profile shows a well-developed seasonal thermocline between the surface and 100-m depth. The standard deviation is high at 20 and 60–80 m (Figure 2*d*), indicating the presence of horizontal inhomogeneities. Below 100 m and down to the bottom the temperature decreases approximately linearly with depth. In this region of the world ocean [*Hecht et al.*, 1988] the changes of salinity with depth are rather important owing to the complicated water mass balance of the Mediterranean. As was stated in the introduction, the basin receives relatively fresh Atlantic water (AW) from the surface inflow at Gibraltar and forms subsurface Levantine Intermediate Water (LIW) through intense evaporation and mixing processes occurring in the Levantine basin. The presence of these two water masses can be traced throughout the Mediterranean basin, and in Figure 2*b* we show their vertical distribution for our data set. The AW is shown by the subsurface salinity minimum located between 20- and 100-m depth. The LIW is contained in a thick layer extending between 100 and 500 m evident by the subsurface salinity maximum. Below 500 m there is a region of transition between LIW and Deep Water (DW) masses. The latter starts at approximately 1200 m as defined by the change in value of the standard deviation of the profile at that depth. Finally, the Brunt-Väisälä profile shows the enhanced stability of the seasonal thermocline region with a well-developed maximum at about 30 m.

It is interesting to notice that the salinity profile shows a

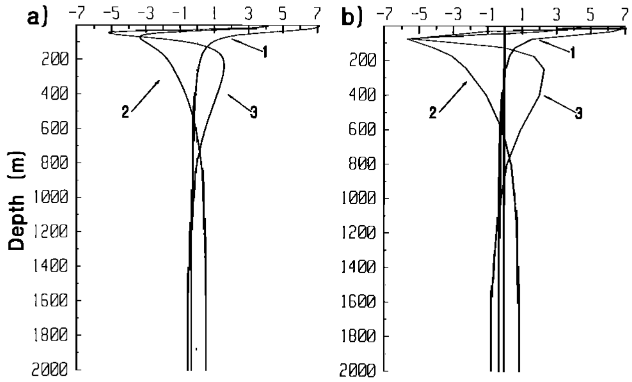

Fig. 3. Dynamical eigenfunctions for the average Brunt-Väisälä frequency profile shown in Figure 2. The numbers indicate the first, second, and third baroclinic mode solutions of equation (1) for (*a*) 2000 levels in the vertical and (*b*) 11 levels in the vertical.

well developed mixed layer in the first 20 m associated with the Surface Ionian Water (SIW) masses. They are clearly formed by intense air-sea interaction processes occurred during the previous summer months. However, the temperature mixed layer is much less clearly defined than the corresponding salinity mixed layer, and its base gently connects to the subsurface layers profile. Thus the salty SIW layer formed during the summer seems then to be more stable than the corresponding temperature layer.

Finally, we have calculated the vertical eigenfunctions for the Brunt-Väisälä frequency profile shown in Figure 2*c*. The vertical eigenfunctions, $\psi_j(z)$, are the solution of the eigenvalue problem

$$\left(\frac{f_0^2}{N^2(z)}\,\psi_{jz}\right)_z = -\lambda_j^2\psi_j \tag{1}$$

with $\psi_{jz} = 0$ at the surface and bottom interfaces located at $z = 0$ m and $z = -2000$ m, the latter being the average depth of the basin of Figure 1*a*. In (1), $f_0 = 2\,\omega \sin\theta_0$, where $\theta_0 = 37°$N is the central latitude of the basin, ω is the Earth's rotation rate, $N^2(z)$ is the Brunt-Väisälä frequency profile of Figure 2*c*, and λ_j is the inverse of the Rossby radius of deformation corresponding to a given baroclinic mode [*Pedlosky*, 1979]. We solved equation (1) with a shooting method and 1 m of vertical resolution. The first three eigenfunctions are shown in Figure 3*a*. The Rossby radii of deformation are 11.8, 5.9, and 4.1 km, respectively, for the first, second, and third baroclinic modes. The first baroclinic mode has a zero crossing at 300 m, and the second has zero crossings at 20 and 650 m.

In order to define the minimum number of levels capable of reproducing the structure of the first three baroclinic modes, we solved equation (1) as a finite difference eigenvalue problem with limited number of levels. We found out that using 11 levels located at 5, 30, 75, 125, 175, 250, 400, 600, 800, 1100, and 1650 m the results were in good agreement with those of the high-resolution method for both ψ_{jz} and λ_j (see Figure 3*b*). Thus in the following we will analyze the physical parameters only at those 11 levels.

4. Correlation Matrix Estimations

The application of the objective analysis technique for mapping various oceanographic parameters requires the representation of the correlation function of the analyzed field. Usually a functional form is used of the kind

$$R(r) = [1 - (r/a)^2]e^{-0.5(r/b)^2} \tag{2}$$

where a is the zero-crossing correlation length scale and b is the e-folding scale. This spatially isotropic and time-independent function has been widely used in previous analyses of POEM data [*Pinardi*, 1988; *Hecht et al.*, 1988; *Robinson et al.*, 1991] and proved to be sufficient for mapping oceanographic fields in the area. Typical values that have been used for a and b are 100 and 67 km [*Robinson et al.*, 1991] or 60 and 40 km [*Hecht et al.*, 1988]. Here, the a and b parameters are computed from the data.

The best approach to estimate the correlation function suitable for mapping a certain parameter (salinity, dynamic height, etc.) at a certain depth is to calculate the correlation matrix of the field to be analyzed and then fit the best (isotropic or not) analytical function.

The definition of the (auto)correlation function of a discrete (de-meaned) series $Z(i)$, $i = 1, n$ is $R(k) = C(k)/C(0)$ where $C(k)$ is the covariance at lag k:

$$C(k) = \frac{\sum_{i=1}^{n-k} Z(i)Z(i+k)}{n-k}$$

For large values of k this estimation of the correlation does not converge because it is multiplied by the ratio $(n - k)/n$. In order to avoid that, one can use the formula

$$R(k) = \frac{\sum Z(i)Z(i+k)}{\left[\sum Z^2(i) \sum Z^2(i+k)\right]^{0.5}}$$

In this way the covariance is normalized by the same data that were used for its estimation; thus the correlation, although slightly biased, converges rapidly. For a two-dimensional series $Z(i, j)$ the estimation of the correlation function is

$$R(k, l) = \frac{\sum Z(i, j)Z(i+k, j+l)}{\left[\sum Z^2(i, j) \sum Z^2(i+k, j+l)\right]^{0.5}}$$

Using this formula, we computed the two-dimensional correlation functions $R(k, l)$ (i.e., the correlation matrices) of temperature, salinity, and dynamic height fields at the 11 levels chosen previously. The bin size used is 75 km, and the calculations were made on nine bins (four positive, four negative, and the zero bin) at each (N-S and E-W) direction. Therefore a 600×600 km^2 domain is represented by each correlation matrix. Since dynamic height was computed with reference level at 2000 m, only the stations deeper than this level were used for the computations. In this way, 110 stations were used for the computation of the central (zero lag) bin, while 25 stations were used for the farthest bin. In Figure 4 the results of those computations are presented for 6 of the 11 levels. These levels were selected as the most representative to describe the variability of the correlation fields at different depths. Note that there is a symmetry

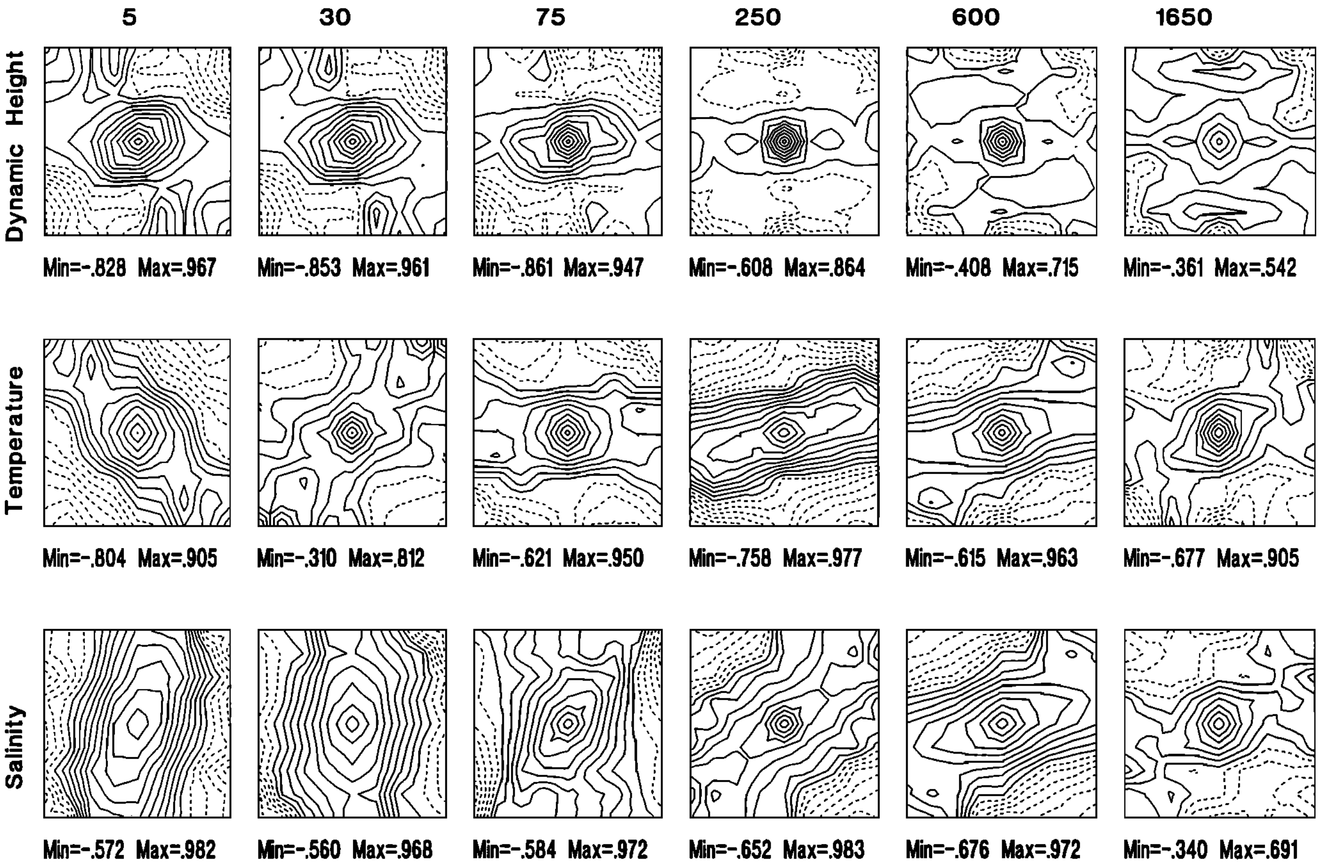

Fig. 4. Correlation matrix for dynamic height, temperature, and salinity at different depths as indicated above the plots. The contour interval is 0.1 everywhere. The domain is 600 × 600 km^2.

around zero of each correlation field artificially produced by the algorithm that is being used.

4.1. *Characteristics of Correlation Fields: Trends*

From the study of the correlation fields of dynamic height at different levels (Figure 4), one can observe a gradual change from the surface to the bottom layers of the correlation ellipse in both size and shape. The size of this ellipse is reduced from the upper to the lower layers, indicating the presence of large-scale features in the surface and AW layers, while at LIW and deeper layers, smaller-scale features dominate. A zonal (E-W) trend is evident in the upper layers, while in deeper layers, features are more isotropic until 1650 m, where a multiple space scale signal emerges.

The same remarks can be made for the temperature and salinity correlation fields. A new feature observed in these fields is the very pronounced trend, present in all levels. This trend rotates clockwise from an almost N-S direction in the surface, to a SW-NE direction in the LIW layers (250 and 600 m). In the deep layers (1650 m) the trend becomes smaller and attains an almost zonal orientation. The fact that this deep trend is not present in the dynamic height field is an indication that at these large scales, temperature and salinity compensate at depth.

4.2. *Correlation Functions*

As was mentioned in the preceding paragraph, the correlation fields of temperature, salinity, and dynamic height indicate that a different correlation function is needed for the objective mapping of those fields at different depths. To estimate this function, one has to choose an analytic formula and then estimate the coefficients of the function by least squares fit on the data.

Although the correlation matrices indicate strong anisotropy in salinity and temperature fields, we decided to use an isotropic function like (2). This procedure is common in objective analysis because large trends present in the data are reproduced well in the objective maps, even if an isotropic correlation function is used [*McWilliams and Owens*, 1976].

Before fitting the function (2) on the correlation matrices, a first-order polynomial trend (i.e., a first-order plane fit in latitude and longitude) was removed from the data and the correlation matrices were recomputed. In this way the fields become less anisotropic and, thus, the computation of the a and b coefficients of the (isotropic) function are more reliable. Examples of detrended correlation fields of salinity and temperature are given in Figure 5. It is obvious that in some cases (e.g., salinity at 75 and 250 m) the trend was not totally removed mainly because it appears in multiple scales and orientations. In any case, the detrended correlation matrices are much more isotropic than the original ones, and thus the fitting of an isotropic function is more trustworthy.

The results of the estimation of the coefficients a and b after the least squares fit of (2) on the azimuthally averaged detrended correlation matrices are presented in Table 1 (missing values indicate scales that exceed 300 km, i.e., zero

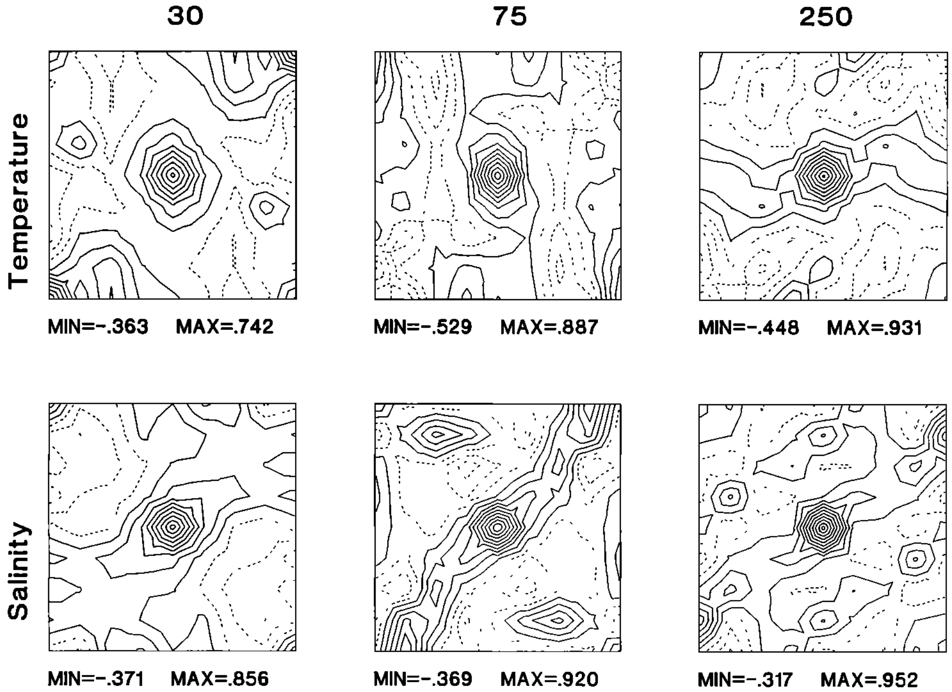

Fig. 5. Detrended temperature and salinity correlation matrix at different depths as indicated above the plots. The contour interval is 0.1 everywhere. The domain is 600 × 600 km^2.

crossing outside the domain). The computations for dynamic height appear to be very stable, with large values of a and b in the upper layers and almost constant (and smaller) values below 175 m. These results are consistent with the features observed in the correlation fields of the dynamic height (Figure 4) i.e., large scales in the upper layers and smaller scales in the lower layers. Three groups of levels with almost the same correlation parameters can be distinguished: (1) the 5- and 30-m levels have characteristic values a = 110, b = 80 km (zero crossing and decay scale respectively); (2) the 75- and 125-m levels have characteristic values a = 90, b = 60 km, and (3) the 175- to 1650-m levels have characteristic values a = 80, b = 50 km. These coefficients were used for the objective analysis of the dynamic height fields.

The computed a and b coefficients for temperature correlation fields at different levels have characteristics similar to those of the dynamic height i.e., large scales in the upper layers and smaller scales below, but a number of irregularities are now present. More specifically, large values of zero-crossing scales are observed at 125, 250, and 400 m. These abnormal values are probably connected to a linear trend that was not successfully removed at those levels. This problem is dominant in the computation of the salinity correlation parameters where in five cases (30, 75, 250, 400, and 1100 m) the zero crossing is undefined. Since this problem makes impossible a proper estimation of the correlation parameters for temperature and salinity, we decided to analyze these fields objectively, using the same a and b values that were computed for the dynamic height field.

TABLE 1. Correlation Parameters at Different Depths

	Dynamic Height		Temperature		Salinity	
Depth, m	a, km	b, km	a, km	b, km	a, km	b, km
5	110	80	120	90	150	100
30	110	70	100	45	···	55
75	90	60	100	70	···	50
125	90	60	180	40	110	80
175	80	50	90	50	40	20
250	80	50	···	50	···	40
400	80	50	140	100	···	60
600	80	50	90	50	40	20
800	80	50	90	50	40	20
1100	70	50	90	40	···	40
1650	75	50	90	50	100	85

5. MAPPING OF PARAMETERS

We analyze now the mapping of dynamic height, temperature, and salinity fields at the same six levels of Figure 4. The dynamic height is referred to 2000 m, the deepest common level to all the CTD stations, which does maintain an adequate number of stations for mapping. We define "gyre" or "eddy" as a region in the maps with an amplitude greater than 1.5 times the standard deviation at that level and with at least one contour closed. We decided to call them "gyres" because all of them are as much as 8–10 times the first Rossby radius of deformation and because our station spacing is insufficient to resolve properly the mesoscale variability of the basin. We consider them general circulation features, following *Robinson et al.* [1991], probably connected to the ocean response to local driving forces (winds, heat and water fluxes) and flow instabilities.

In Figure 6 the dynamic height fields show a total of six anticyclones and one cyclone. Three of these anticyclones are evident from the surface layers (30–75 m), and three of them appear only in the LIW and DW layers. These fields show very clearly the decrease with depth of the spatial scales of the variability. South of 37°N the flow is dominated by a large area of anticyclonic circulation with three anticyclonic gyres embedded in it. The cyclonic flow field surrounding the anticyclonic area is weak except along the western sides of the basin, but the deep reference level significantly reduces the number of available stations in the area and consequently does not allow us to describe properly the flow there.

In Table 2 we summarize the gyre characteristics for all the parameters mapped in Figure 6. It is interesting to notice the subsurface signature of the double gyre feature A2 + A4. This feature is the strongest of the gyres with respect to the standard deviation at each level from 250 m down. The three anticyclones A1, A3, and A5 on the western Ionian side have a particularly significant amplitude in the upper LIW and AW levels, except for A3 which is significant also at the deepest level. Thus the three gyres embedded in the large-scale anticyclonic general circulation flow have different vertical structures and probably origin, as we will also see in the EOF analysis section.

The temperature and salinity fields of Figure 6 also show a decrease of the spatial scales with depth. We have nine temperature gyres, six anticyclones and three cyclones, and five salinity gyres, three highs and two lows. The gyres are below the 1.5 standard deviation threshold at all surface levels where the flow is dominated by a smooth general circulation field which composes the large-scale trends of the correlation matrices. Note the familiar E-W trend in the salinity field at the upper layers due to the AW entering the Ionian Sea from Sicily and saltier surface waters in the eastern side. In addition, the temperature field shows the well-known N-S upper layer gradient. However a new aspect in the temperature and salinity fields is revealed, which is the large Peloponnesian region high values of T and S with respect to the rest of the basin. This feature has been also described by *Robinson et al.* [1991] in the analysis of the dynamic height fields only. Overall, the large scale T-S contrast in the Ionian is composed of gyres which are several standard deviations away from the mean at each level. For example, embedded in the AW portion of the water masses of the basin there are intense subsurface "light gyres" like S2, which protrudes in the vertical down to 250 m, well below the vertical position of AW as indicated by the average profile of Figure 2*b*. It is a vertical plume of AW (corresponding to the T6 low-temperature gyre) which is clearly seen in the section at 37°N of Figure 7.

We notice also that the salinity gradients become zonal from 250 m down as in the temperature field. Since the salinity and temperature large-scale gradients have the same sign, they will give almost no net current flow as is shown in the dynamic height field of Figure 6. The only contribution to the velocity field below 250 m comes from the gyre T and S anomalies. This behavior is similar to what happens at the Mediterranean salt tongue in the North Atlantic. A very clear salinity and temperature anomaly in the eastern North Atlantic associated with the Gibraltar outflow of Mediterranean waters can be distinguished. However no circulation is associated with these strong T and S anomalies, since they compensate in the equation of state. Thus the heat and water fluxes responsible for the formation of Mediterranean waters such as LIW and TW do not drive any direct baroclinic circulation except at the level of the subbasin gyres.

The dynamic height gyres A2 and A4 correspond to the strongest temperature (T4 and T8) and salinity (S3 and S4) gyres below 250 m. It is evident that the water mass properties of A2 and A4 are consistent with the transition water mass layer characteristics, with a tendency for salinity and temperature to compensate because the salinity and temperature anomalies are of the same sign. These two gyres contain the saltiest and warmest water masses of the overall northern Ionian basin, perhaps hinting at the presence of a distinct water mass source, probably in the Aegean Sea. In Figure 7 we show the section along 36°N which cuts through A1, A3, and A2. The deepest gyres (A2 and A3) are capped at the surface by the steep thermocline between 50 and 100 m and extend below 500 m (not shown). Above 500 m, A2 is formed only by a sharp isotherm displacement, but below 500 m the salinity anomaly is relevant as well, giving a net contribution to the density anomaly of the gyre. Thus below the LIW average layer (see Figure 2*e*) and inside the gyres A2 and A4 there is another relative salinity maximum which must be associated with a different water mass belonging to the TW layer.

Finally, we notice in Figure 7 the plume of low salinity and temperature centered on station 4021. This T-S anomaly, however, is totally absent in the dynamic height field owing to compensation between salinity and temperature anomalies in the equation of state for density. It appears that the compensation processes occur at all different spatial scales, from the gyre scale to the overall basin scale as discussed above.

6. EOF Representation of Data

Empirical orthogonal functions are an efficient way to represent a field of physical parameters [*Fukumori and Wunsch*, 1991]. They are the optimal decomposition (in a least squares sense) of a parameter field into its principal components to help the interpretation and reconstruction of data with the smallest number of degrees of freedom. Thus we take our objectively analyzed data at the 11 levels of section 2 and we decompose the scalar field, Φ, in its vertical EOF components, $\Psi_j^{\mathrm{eof}}(z)$ with $j = 1, \cdots, n$, and their respective horizontal amplitudes, $\alpha_j^{\mathrm{eof}}(x, y)$, e.g.,

$$\Phi(x, y, z) = \sum_{j=1}^{n} \Psi_j^{\mathrm{eof}}(z)\alpha_j^{\mathrm{eof}}(x, y) \qquad (3)$$

The Ψ fields are the eigenfunctions of the (auto)covariance matrix A_{kl}, $k, l = 1, \cdots$, number of levels defined for a three-dimensional discrete scalar field $\Phi(i, j, k)$

$$A_{ij} = \frac{(\Phi_i\Phi_j)}{N[(\Phi_i^2)(\Phi_j^2)]^{0.5}}$$

In Figure 8*a* we show the shape of the first three Ψ^{eof} for the dynamic height field. They account for 70%, 24%, and 5% of the variance. In Figures 8*b* and 8*c* the α^{eof} are shown for the first two modes. It is then evident that the first EOF accounts for the subsurface intensified gyres while the second EOF captures the surface layers variability and the zonal trend in the dynamic height field. However, it does not discriminate between the various subsurface gyres, probably on account of the coarse subsampling of the field in vertical.

In Figure 9*a* we show the first three EOFs for the temperature field. Again the first EOF attains large amplitudes at the subsurface layers and accounts for 60% of the

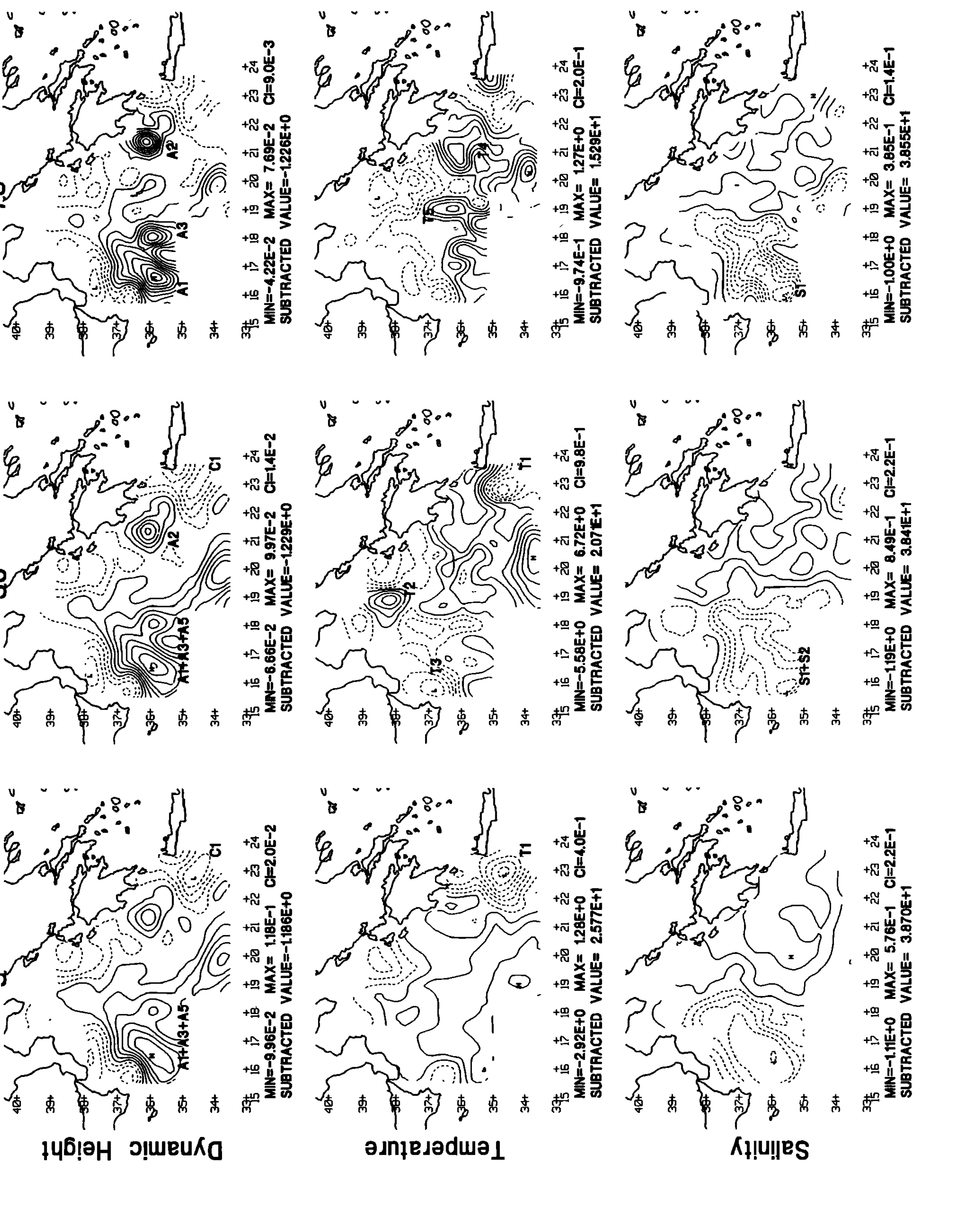
Dynamic Height
Temperature
Salinity
5
30
75
A1+A3+A5
C1
A2
A3
A1
T1
T2
T3
S1+S2
S1
MIN=-9.96E-2 MAX= 1.18E-1 CI=2.0E-2
SUBTRACTED VALUE=-1.186E+0
MIN=-2.92E+0 MAX= 1.28E+0 CI=4.0E-1
SUBTRACTED VALUE= 2.577E+1
MIN=-1.11E+0 MAX= 5.76E-1 CI=2.2E-1
SUBTRACTED VALUE= 3.870E+1
MIN=-6.66E-2 MAX= 9.97E-2 CI=1.4E-2
SUBTRACTED VALUE=-1.229E+0
MIN=-5.58E+0 MAX= 6.72E+0 CI=9.8E-1
SUBTRACTED VALUE= 2.071E+1
MIN=-1.19E+0 MAX= 8.49E-1 CI=2.2E-1
SUBTRACTED VALUE= 3.841E+1
MIN=-4.22E-2 MAX= 7.69E-2 CI=9.0E-3
SUBTRACTED VALUE=-1.226E+0
MIN=-9.74E-1 MAX= 1.27E+0 CI=2.0E-1
SUBTRACTED VALUE= 1.529E+1
MIN=-1.00E+0 MAX= 3.85E-1 CI=1.4E-1
SUBTRACTED VALUE= 3.855E+1

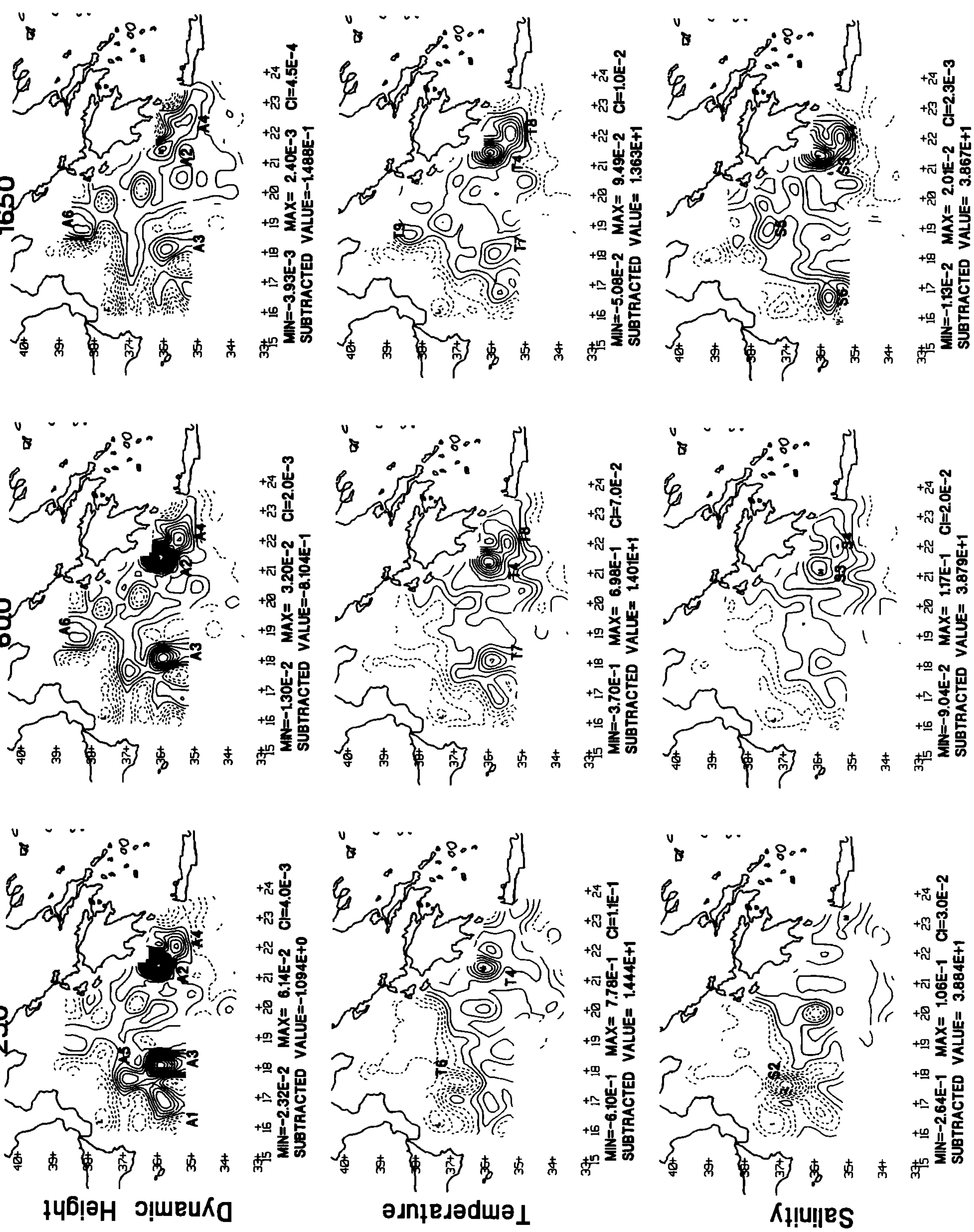

Fig. 6. Dynamic height, temperature and salinity objective fields at different depths indicated above the plots. The contour interval is chosen to be one-half the standard deviation at each level.

TABLE 2. General Circulation Gyre Names

Dynamic Height		Temperature		Salinity		
Gyre	Levels of Extension, m	Gyre	Levels of Extension, m	Gyre	Levels of Extension, m	Water Mass Composition
A1	75–1650			S1 (−)	75–250	LIW
A2	30–1650	T4 (+)	75–1650	S3 (+)	600–1650	LIW + TW
A3	75–1650	T7 (+)	400–1650			TW
A4	125–800	T8 (+)	600–1650	S4 (+)	600–1650	TW
A5	175–400	T6 (−)	125–250	S2 (−)	175–400	AW
A6	1100–1650	T9 (+)	1650			DW
C1	5	T1 (−)	5			SIW
		T2 (+)	30			AW
		T3 (−)	30			AW
		T5 (+)	75			AW
				S5 (+)	1650	DW

Pluses and minuses indicate positive and negative amonalies at the given levels. Blanks indicate the absence of a gyre in the corresponding parameter.

variance. The first projection coefficient shown in Figure 9*b* shows by consequence the subsurface temperature gyres, T4, T7, and T8. The second EOF accounts for 16% of the variance and its α_2^{eof} (Figure 9*c*) shows the LIW-intensified gyres like T6 and again T7 and T4. We point out that the first EOF corresponds to an almost vertically constant temperature profile (from 100 m down) and the second to a change of sign at 350 m. This change of sign is well understood for the case of T6, which is a weak, almost positive anomaly above 250 m (see Figure 6) and a negative anomaly below it. The third EOF accounts still for 10% of the variance, and we have to use as many as seven EOFs to get 99% of the signal variance. The temperature vertical variance resides then in higher vertical modes than the dynamic height field owing to the compensation processes with salinity described before.

Finally, in Figure 10*a* we show the first three EOFs for the salinity parameter. They account for 62%, 20%, and 8% of the variance, respectively. Again the first EOF shows a

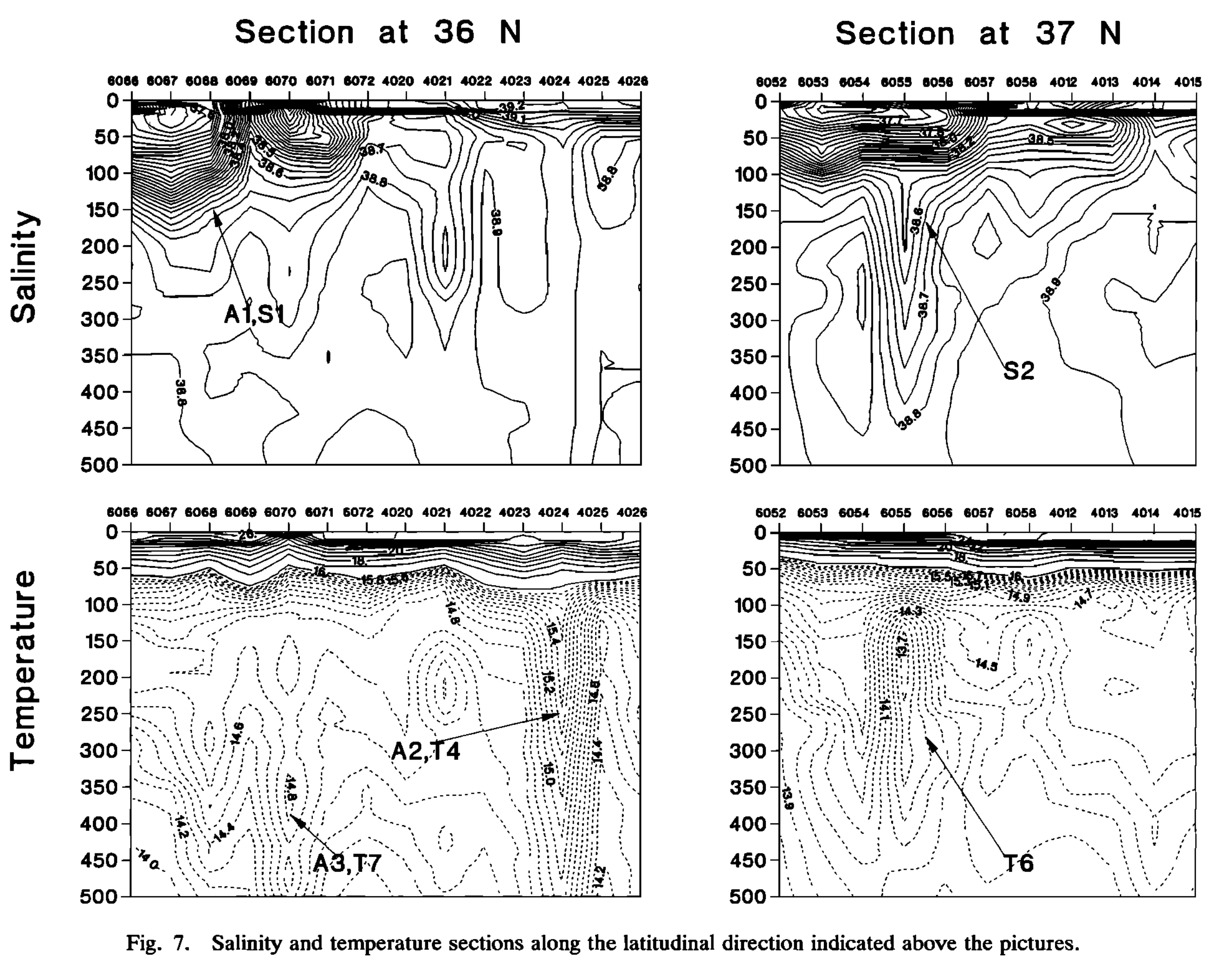

Fig. 7. Salinity and temperature sections along the latitudinal direction indicated above the pictures.

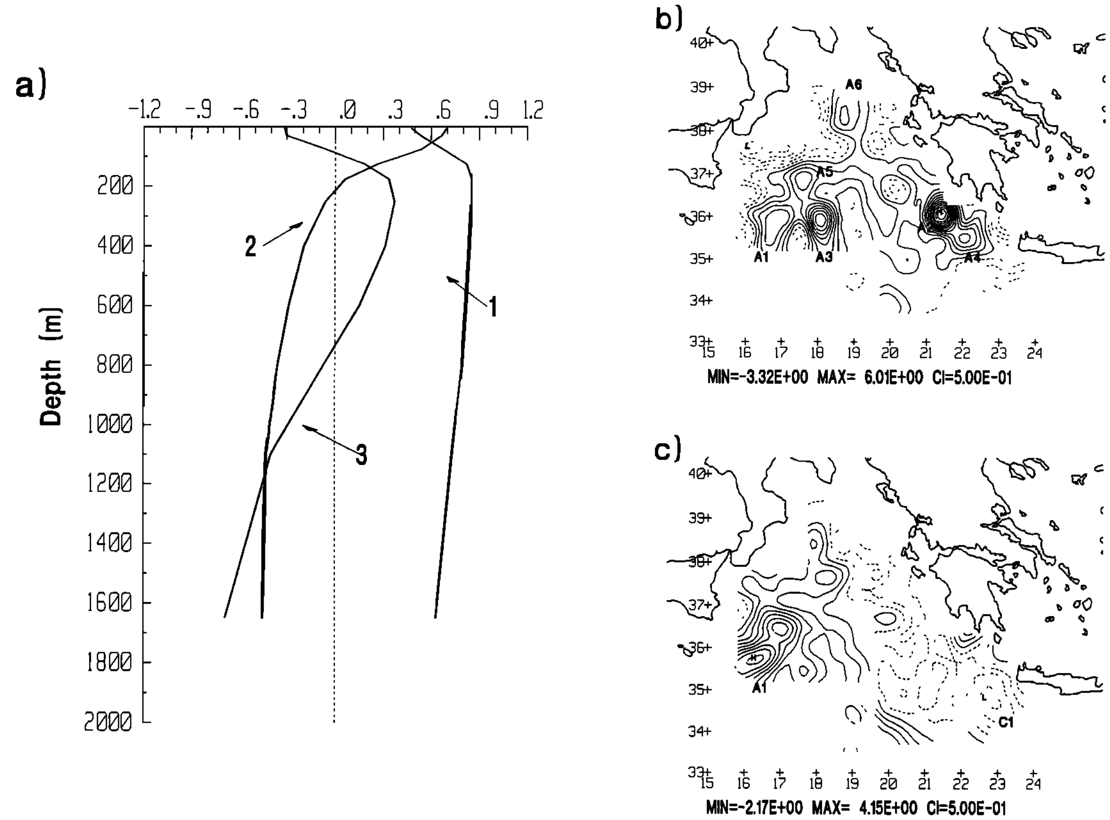

Fig. 8. (*a*) The first three EOFs of dynamic height, and the amplitude of (*b*) mode 1 and (*c*) mode 2.

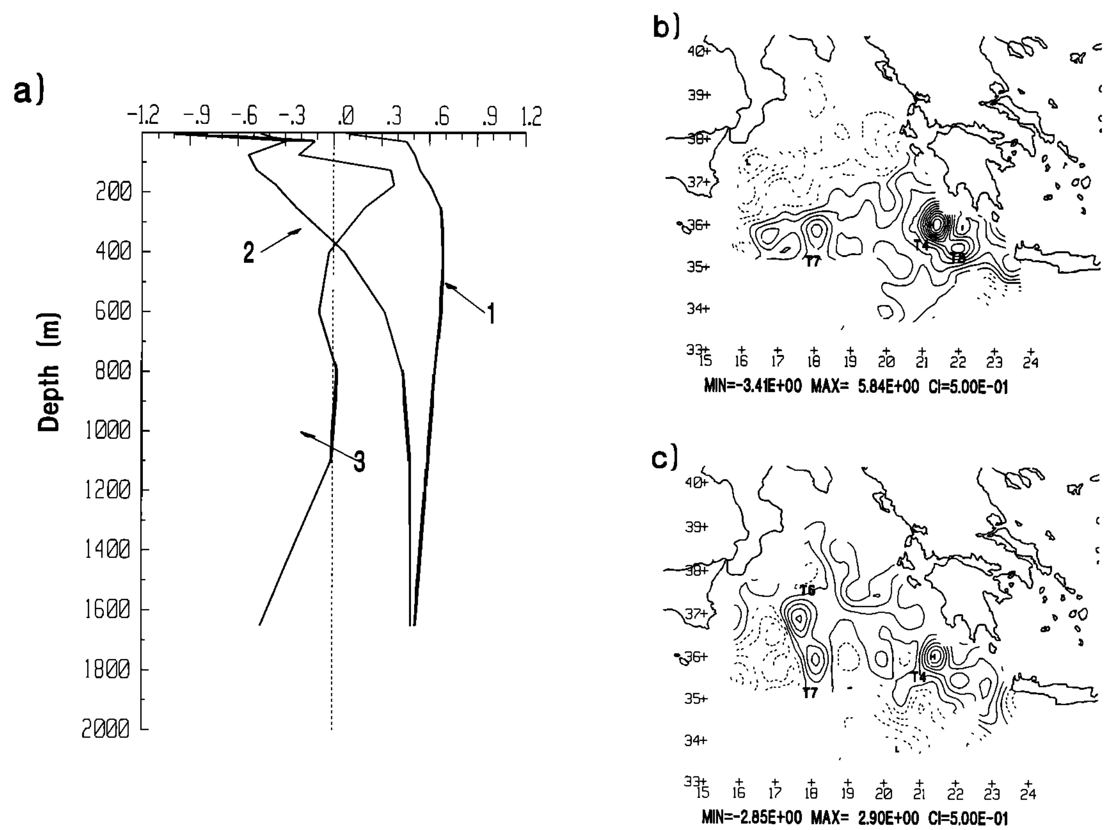

Fig. 9. (*a*) The first three EOFs of temperature, and the amplitude of (*b*) mode 1 and (*c*) mode 2.

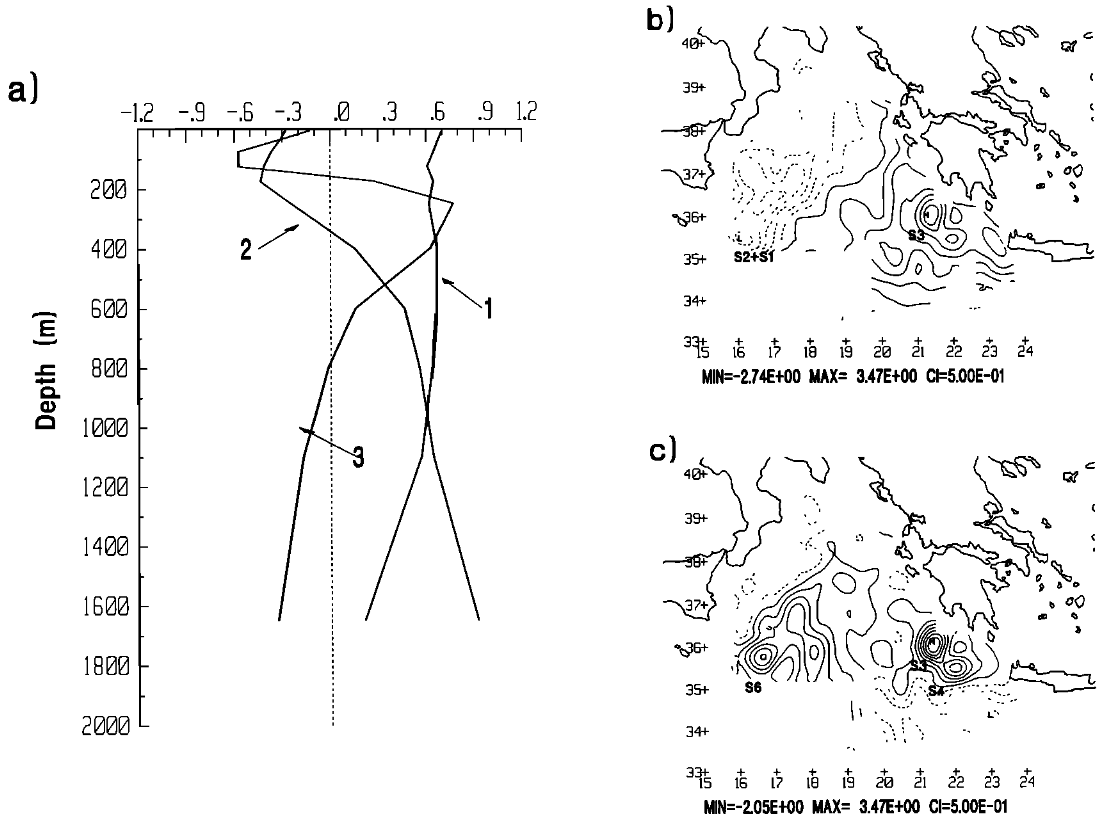

Fig. 10. (*a*) The first three EOFs of salinity and the amplitude of (*b*) mode 1 and (*c*) mode 2.

vertically coherent salinity field from the surface down to 1200 m which is shown in Figure 6 by the vertical coherence of the large-scale E-W trend component. The first EOF in fact includes principally this large-scale trend and the overwhelming signal of S3. The second EOF captures the smaller-scale gyres of the salinity, e.g., S3, S4, and S6. The interesting S2 gyre of AW has such a high modal structure that it is not represented by any of the first two projection coefficients (Figures 10*b* and 10*c*). Another interesting difference between the temperature and salinity EOFs is that the second salinity EOF is clearly bottom intensified, thus trying to capture the TW layer variance. This is very special for the salinity parameter and it indicates the presence of the peculiar variability in the salinity field associated with TW anomalies. This is another possible piece of evidence for distinct water mass anomalies below the LIW layer of probable Aegean origin. The third salinity EOF describes the LIW-intensified variability (e.g., S2) and is not shown.

To show the ability of the first two EOFs to reproduce the variance at each level, we proceed to calculate the variance of the residual field $\Phi'(x, y, z)$ defined as

$$\Phi' = \Phi - \alpha_1^{\text{eof}}\Psi_1^{\text{eof}} - \alpha_2^{\text{eof}}\Psi_2^{\text{eof}}$$

This will account for the reliability of the fit of the physical parameters only on two EOFs. In Figure 11*a* we show the variance of Φ' at each level for the dynamic height. The fit is extremely good except for the deeper level at which the leftover variance is about 20%. This is understandable since it was evident from Figure 8*a* that the deepest level variance was accounted for by the third EOF, which is in fact intensified at 1650 m. Thus even though the third EOF accounts only for 5% of the total water column variance, the error resulting from neglecting that mode at a single level can be much higher.

The temperature field residual variance (Figure 11*b*) is surface intensified because both the large-scale N-S gradient and the surface T1 gyre are absent from α_1 and α_2 (see Figures 9*b* and 9*c*). These features must appear in higher modes, and in fact the third mode, as shown in Figure 9*a*, is surface intensified and almost zero elsewhere. This shows the amplitude of the large-scale trend to be maximum at the mixed layer levels (above 75 m) and almost absent below. The residual variance at 5 and 30 m due to the omission of the third mode is now as high as 70% and 50%.

The salinity field residual variances (Figure 11*c*) are as high as for the temperature fit at the subsurface levels. This time the surface is well represented, but the LIW level variance is not taken into account by the first two modes as well as the other levels. This is congruent with the shape of the third EOF, which was omitted by the fit and has maximum amplitude at 250 m.

In conclusion, the fit of the first two EOFs on the dynamic height, temperature, and salinity profiles shows that the easiest parameter to represent is the dynamic height, which has high variance in the first and second modes only. The latter are either homogeneous (below 100 m) or first baroclinic modelike (Figure 8*a*). The first EOF amplitude α_1 captures the gyre fields while the second α_2 the large scale E-W trend of the Ionian basin surface general circulation. In contrast, to describe salinity and temperature features, it is necessary to add at least the third or higher modes. The difference between the dynamic height and the T and S field

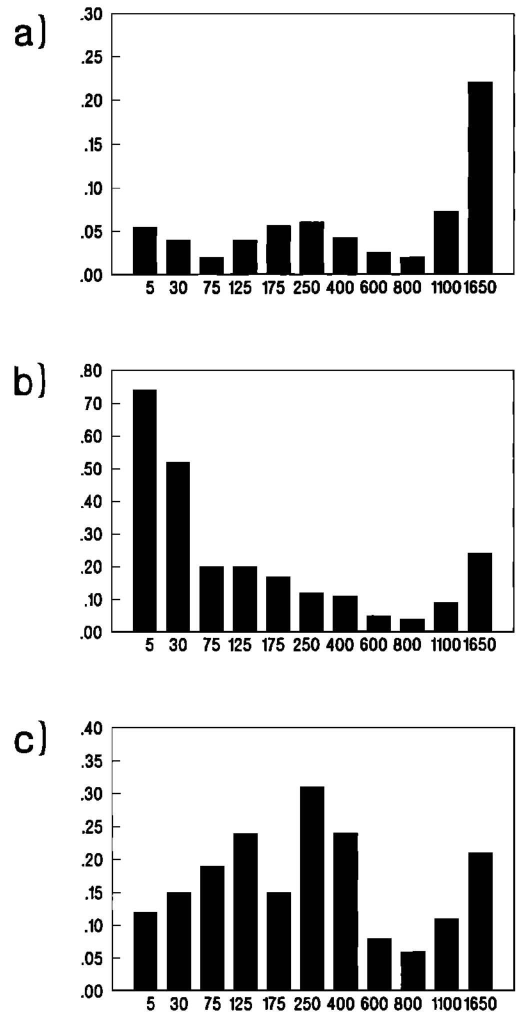

Fig. 11. Residual variance from the projection on the first two EOF modes of (*a*) dynamic height, (*b*) temperature, and (*c*) salinity at different levels.

fit is due to the compensation effects between T and S in the equation of state.

7. CONCLUSIONS

In this paper we have studied the summer 1987 flow field in the Ionian Sea. The high quality of the data set allowed, for the first time, an extensive and consistent analysis of its spatial variability and dynamical structure.

The results show that the spatial scales of the variability decrease with depth. The gyre-scale motions are evident only in the deeper than AW layers, where the large-scale temperature and salinity anomalies compensate. In contrast, the surface flow field is dominated by large-scale motions produced by noncompensating T and S trends. We argue that this is indicative of the direct large-scale driving by heat and water fluxes at the surface which do not penetrate to deep layers.

The dynamic height field is dominated by a large-scale anticyclonic flow field south of 37°N and a strong anticyclonic double-gyre feature south of the Peloponnesian peninsula. A total of one cyclone and six anticyclones are found in the baroclinic current field. Three of them are embedded in the large-scale anticyclonic flow field south of 37°N, although they are probably of different origin since their cores are formed by different water masses. One of them (A5) is formed by a vertical plume of AW which extends down to 250 m, well below the basin average position of this water mass layer.

The largest temperature, salinity, and dynamic height anomaly of the summer northern Ionian general circulation is by far the Peloponnesian double gyre, which is formed by a large temperature anomaly above 500 m and a large salinity anomaly below. This structure indicates that different water masses are contributing to this anticyclonic flow field, the deepest being probably of Aegean origin.

The vertical EOF analysis of the dynamic height field indicates that two EOFs can account for more than 90% of the variance at each single level except for the deepest one considered (1650 m). This is because the third EOF mode is bottom intensified. The projection into vertical EOFs of the dynamical height fields clearly distinguished the spatial scales explained by each mode; the gyres are contained in the first EOF, while the surface large-scale flow field is contained in the second.

The T and S EOFs are different from the EOF of the dynamic height field because of the compensating effects between T and S. First, to describe T and S for more than 90% of the variance, we need up to seven vertical EOF modes. Second, large-scale trends and gyres are not clearly separated by different vertical EOFs as they were for the dynamic height fields.

In conclusion this data analysis has shown that the horizontal (decorrelation scale) and vertical (EOF) structure of the northern Ionian Sea flow field is intensified at the level of subbasin-scale gyres. They totally mask the larger scale trends in T and S which horizontally compensate at the basin scale below 250-m depth. The spatial scales of the general circulation are of the order of 100 km horizontally and several hundred meters in the vertical.

Acknowledgments. We are thankful to A. Michelato, A. Theocharis, A. Artegiani and D. Bregant for making the data available to us. This work was partially funded by the EEC MAST contract 0039-C "MERMAIDS."

REFERENCES

Fukumori, I., and C. Wunsch, Efficient representation of the North Atlantic hydrographic and chemical distributions, *Prog. Oceanogr.*, *27*, 111–195, 1991.

Hecht, A. Z., N. Pinardi, and A. Robinson, Currents, water masses, eddies and jets in the Mediterranean Levantine basin, *J. Phys. Oceanogr.*, *18*, 1320–1353, 1988.

Malanotte-Rizzoli, P., and R. A. Robinson, POEM: Physical oceanography of the eastern Mediterranean, *Eos Trans. AGU*, *69*, 194–203, 1988.

McWilliams, J. C., and W. B. Owens, Estimation of spatial covariances from the mid-ocean dynamics experiment, *Tech. Note NCAR/TN-115+STR*, 25 pp., Natl. Cent. for Atmos. Res., Boulder, Colo., 1976.

Miller, A. R., Physical oceanography of the Mediterranean Sea: A discourse, *Rapp. P. V. Reun. Comm. Int. Explor. Sci. Mer Mediterr.*, *17*, 857–871, 1963.

Ovchinnikov, I. M., The formation of intermediate water in the Mediterranean, *Oceanology*, Engl. Transl., *24*, 168–173, 1984.

Ovchinnikov, I. M., and A. F. Fedoseyev, The horizontal circulation of the water of the Mediterranean Sea during the summer and winter seasons, in *Basic Features of the Geological Structure, Hydrological Regime and Biology of the Mediterranean*, edited by L. M. Fomin, translated from Russian by the Institute for

Modern Languages, pp. 185–201, U.S. Naval Oceanographic Office, Stennis Space Center, Miss., 1965.

Ovchinnikov, I. M., and Y. A. Plakhin, Formation of the intermediate waters of the Mediterranean Sea in the Rhodes cyclonic gyre, *Oceanology*, Engl. Transl., *24*, 317–319, 1984.

Ozsoy, E., A. Hecht, and U. Unluata, Circulation and hydrology of the Levantine Basin, Results of POEM coordinated experiments 1985–1986, *Prog. Oceanogr.*, *22*, 125–170, 1989.

Pedlosky, J., *Geophysical Fluid Dynamics*, 624 pp., Springer-Verlag, New York, 1979.

Pinardi, N., Report of the POEM mapping group: August/September 1987: General circulation survey data set representation, *Tech. Rep. 1-88*, Ist. per lo Stud. dello Metodol. Geofis. Ambientali, Cons. Naz. delle Ric., Modena, Italy, 1988.

Robinson, A. R., M. Golnaraghi, W. G. Leslie, A. Artegiani, A. Hecht, E. Lassoni, A. Michelato, E. Sansone, A. Theocharis, and U. Unluata, The eastern Mediterranean general circulation: Features, structure and variability, *Dyn. Atmos. Oceans*, *15*, 215–240, 1991.

Schlitzer, R., W. Roether, H. Oster, H. Junghans, M. Hausmann, H. Johannsen, and A. Michelato, Chlorofluoromethane and oxygen in the eastern Mediterranean, *Deep Sea Res.*, *38*(12), 1531–1551, 1991.

UNESCO (United Nations Educational, Scientific, and Cultural Organization), Physical oceanography of the eastern Mediterranean: An overview and research plan, *UNESCO Rep. Mar. Sci. 30*, 36 pp., Paris, 1984.

A. Lascaratos and K. Nittis, Laboratory of Meteorology and Oceanography, Department of Applied Physics, University of Athens, 33 Ippocratous Street, 10680 Athens, Greece.

N. Pinardi, IMGA-CNR, Via Emilia Est 770, 41100 Modena, Italy.

(Received February 21, 1992;
revised October 29, 1992;
accepted January 26, 1993.)